# Position Sensor Fault Detection of IPMSM Using Single DC-Bus Current Sensor with Accuracy Uncertainty

Jiadong Lu, Yihua Hu, *Senior Member, IEEE,* Jinglin Liu, *Member, IEEE,* Xiaokang Zhang, Chun Gan, *Member, IEEE*, and Zheng Wang, *Senior Member, IEEE*

***Abstract*—This paper proposes a position sensor fault detection scheme using single DC-bus current sensor for interior permanent magnet synchronous motor (IPMSM) drives. The three-phase current values are derived from the only DC-bus current sensor, and the accuracy uncertainty of the current sensor is also considered. The six active vectors are divided into three groups for the purpose of sensor calibration ~~purposes~~. Then, the proposed DC-bus current sensor offset error calibration method is implemented by setting two opposite basic vectors ~~together~~ simultaneously and measuring the two current values on both sides of the junction point ~~for~~ in the same time interval. If the sum of the two sampled current values is not zero, it indicates that the offset error of the DC-bus current sensor ~~can be detected~~exists ~~and compensated~~. Therefore, a corresponding compensation method is proposed. Meanwhile, the DC-bus current slopes under different switching states are closely related to the rotor position, which are utilized for position sensor error detection. Finally, the effectiveness of the proposed scheme is verified by experimental results on a 5-kW IPMSM motor prototype.**

***Index Terms*—Accuracy uncertainty, error compensation, fault detection, fault tolerant control, interior permanent magnet synchronous motor (IPMSM).**

## I. Introduction

INTERIOR permanent magnet synchronous motors (IPMSMs) are now widely used in industrial applications due to the outstanding features and excellent controlling performances [1]-[4]. Usually, an IPMSM drive system contains several kinds of sensors, of which the ~~most important are~~ position ~~sensor~~ and current sensors are of paramount significance [5]. Thanks to these high-precision sensors, the advantages of IPMSM can be ~~achieved~~revealed. However, after a long time of use, especially near the end of ~~its~~ life-span period, or ~~works~~ under a harsh working condition, the accuracy of these sensors ~~will~~ decreases. ~~A bad result followed by this is that~~In this case, the controlling performance~~s~~ of the drive system will be compromised, leading to~~such as~~ speed fluctuations, torque ripple, and unbalanced three-phase currents [6]-[11].

Take ageing and temperature drift ~~for~~ into consideration, the accuracy of both the current and position sensors in the drive system is degraded. For current sensors, the main types of errors are offset ~~error~~ and scaling errors [5], which cause periodic speed ripples ~~of~~ with one and two times the fundamental current frequency respectively [9]. The influence of current measurement error on the system performance ~~are~~ is analyzed ~~detailedly~~ in detail in [5], and the compensation strategies are proposed for current and speed sensor errors. However, the proposed scheme will become invalid if there is no healthy current sensor in the drive system. Papers [6] and [10] propose methods to compensate the offset and scaling errors separately without any additional hardware, while~~but using~~ the commanded voltage reference of the current controller is applied. However, several additional digital signal filters have to be added in the method, which increases the ~~amount of computation~~computational burden and system complexity. For some special applications such as EVs, emergency parking is not the best way ~~to solve~~of dealing with the current sensor failures [8]. Therefore [NK1] , control strategies are proposed in the event of current sensor failure [8], [11], [12].

For position sensors, the commonly occurred faults are pulse loss and periodic signal interference, which cause undesired speed fluctuation, torque ripple, and unbalanced three-phase currents. The hall-effect position sensor fault detection, identification, and compensation strategy ~~is~~ are discussed detailedly in [13[NK2]]. The information of the estimated rotor position and speed ~~information~~, which ~~are~~ is used as the criterion ~~for~~ under the situation of ~~the~~ hardware fault, have uncertain error limits according to the operation status and system parameters. Therefore[NK3], an observer based position sensor fault detection method with adaptive threshold is proposed in [14]. Two active fault-tolerant control schemes for EV or HEV applications are proposed in [15]. The sensorless control technologies ~~have been~~are proposed and studied for decades [16]-[21], which ~~have~~ achieve~~d~~ ~~good~~ precise estimation results. Whereas, the accuracy of the proposed methods ~~is guaranteed by~~depends on the accuracy of the current sensors.

In [5], the speed sensor fault detection and compensation method is proposed by considering current sensor errors. However, if no accurate current sensor exists in the system, the proposed strategy will become invalid. ~~An a~~Adaptive position and current estimators are proposed in [22], which are robust to motor parameter~~s~~ change. However, the proposed method relies on the search coil, which requires special ~~changes~~ modifications in the motor structure.[NK4] Detection[NK5] and isolation strategies of both position and current sensor faults are proposed in [23], [24].

The phase current reconstruction strategies are researched in [25]-[29]. However, the current sensor errors are not taken into consideration in these literatures. The DC offset error is compensated in [30], whereas the proposed strategy utilizes digital filters and a proportional-integral (PI) controller which ~~is~~ makes the circuit structure complicated.

As illustrated in Fig.1, for cost efficiency and fault-tolerance capability considerations, a single DC-bus current sensor is applied in the system with no phase current sensor~~s~~ installed. The three-phase currents are reconstructed from the DC-bus current values (in Fig.1, block "Recon."). If no error exists in the DC-bus current sensor, the accurate three-phase currents can be obtained continuously. And the position sensor fault detection and calibration strategy can be well implemented (in Fig.1, block "Calibration"). However, if the accuracy uncertainty of the DC-bus current sensor is taken into consideration as shown in Fig.1, the ~~utilization~~ method of utilizing the DC-bus current information for detecting and calibrating ~~of~~ the position sensor fault ~~will be affected or even~~may become invalid. Also, undesired errors are encountered in the reconstructed three-phase currents ~~will show undesired errors~~. ~~All of these consequences will have a bad effect on the system.~~

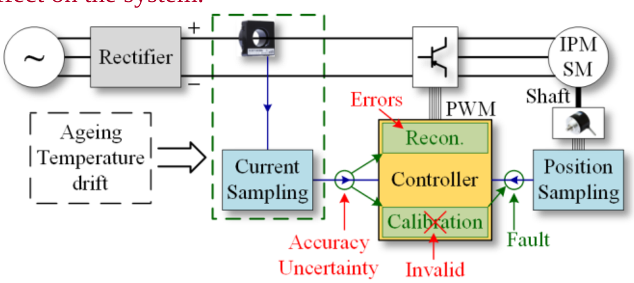


Fig. 1. Influence of DC-bus current sensor accuracy uncertainty on system performance.

In this paper, the position sensor fault detection strategy using single DC-bus current sensor with accuracy uncertainty is proposed, where the three-phase current values are also obtained in the current reconstruction process. The proposed DC-bus offset error calibration method is implemented by setting two opposite basic vectors ~~together~~ simultaneously and measuring the two current values on both sides of the junction point ~~for~~ in the same time interval. Under this circumstance, the sum of the two current values should be zero. However, if the value is not zero, the offset error of the DC-bus current sensor will be detected, which can be calculated as the average value of the two sampled currents. The DC-bus current slopes under different switching states are closely related to the rotor position, which can be used for position sensor error detection.

This paper is organized as follows. In Section II, the DC-bus offset error calibration strategy is illustrated. In Section III, the position sensor fault detection strategy using DC-bus current slope measurement is proposed and the effect of scaling error in the DC-bus current sensor on the position sensor fault detection is analyzed accordingly. In Section IV, the PWM synthesis method and the overall control strategies are proposed and discussed. In Section V, experimental results are presented. Finally, ~~The~~ the conclusion is given ~~finally~~.

## II. Proposed DC-Bus Current Sensor Offset Error Calibration Method

The mathematical model of IPMSM is given by [20]

$$\begin{bmatrix}u_\alpha\\ u_\beta\end{bmatrix}=R\cdot\begin{bmatrix}i_\alpha\\ i_\beta\end{bmatrix}+\begin{bmatrix}L_0+L_2\cos2\theta & L_2\sin2\theta\\ L_2\sin2\theta & L_0-L_2\cos2\theta\end{bmatrix}\times\frac{\mathrm{d}}{\mathrm{d}t}\begin{bmatrix}i_\alpha\\ i_\beta\end{bmatrix}+\frac{\mathrm{d}\theta}{\mathrm{d}t}\left(2L_2\begin{bmatrix}-\sin2\theta & \cos2\theta\\ \cos2\theta & \sin2\theta\end{bmatrix}\begin{bmatrix}i_\alpha\\ i_\beta\end{bmatrix}+\psi_f\begin{bmatrix}-\sin\theta\\ \cos\theta\end{bmatrix}\right) \tag{1}$$

$$\begin{bmatrix}L_0\\ L_2\end{bmatrix}=\frac{1}{2}\begin{bmatrix}1 & 1\\ 1 & -1\end{bmatrix}\cdot\begin{bmatrix}L_\mathrm{d}\\ L_\mathrm{q}\end{bmatrix} \tag{2}$$

where $u_{\alpha,\beta}$ and $i_{\alpha,\beta}$ are the motor voltages and currents in the α-β ~~axis~~ reference frame, respectively; $R$ is the winding resistance; $L_{\mathrm{d,q}}$ denotes the winding inductances in the d-q ~~axis~~ reference frame; $\theta$ is the rotor electrical angle; $\psi_f$ is the permanent magnet (PM) flux linkage.

The input voltage vector is usually synthesized by the six basic active vectors ($V_{100}$, $V_{110}$, $V_{010}$, $V_{011}$, $V_{001}$, $V_{101}$) and two basic zero vectors ($V_{000}$ and $V_{111}$). When analyzing the model excited by different basic active vectors in (1), the current derivative values in the three-phase static reference frame can be simplified as [3]

$$\frac{\mathrm{d}}{\mathrm{d}t}\begin{bmatrix}i_\mathrm{A}\\ i_\mathrm{B}\\ i_\mathrm{C}\end{bmatrix}=\frac{2}{3L_\mathrm{d}L_\mathrm{q}}\cdot\mathbf{X}\cdot\begin{bmatrix}u_\mathrm{A}\\ u_\mathrm{B}\\ u_\mathrm{C}\end{bmatrix} \tag{3}$$

$$\mathbf{X}=\begin{bmatrix} a & -\frac{a}{2}+\frac{\sqrt{3}c}{2} & -\frac{a}{2}-\frac{\sqrt{3}c}{2}\\ -\frac{a}{2}+\frac{\sqrt{3}c}{2} & \frac{a}{4}-\frac{\sqrt{3}c}{2}+\frac{3b}{4} & \frac{a}{4}-\frac{3b}{4}\\ -\frac{a}{2}-\frac{\sqrt{3}c}{2} & \frac{a}{4}-\frac{3b}{4} & \frac{a}{4}+\frac{\sqrt{3}c}{2}+\frac{3b}{4}\end{bmatrix} \tag{4}$$

$$\begin{cases} a=L_0-L_2\cos2\theta\\ b=L_0-L_2\cos2\theta\\ c=L_2\sin2\theta\end{cases} \tag{5}$$

where $u_{\mathrm{A,B,C}}$ and $\mathrm{d}i_{\mathrm{A,B,C}}/\mathrm{d}t$ are the input voltages and output current derivative values in the A-B-C ~~axis~~ reference frame, respectively.

In (3), $u_{\mathrm{A,B,C}}$ varies with ~~different~~ the switching states as shown in Table I. In the table $U_{\mathrm{DC}}$ represents the input DC-bus voltage, $V_{000}$, $V_{100}$, $V_{110}$, $V_{010}$, $V_{011}$, $V_{001}$, $V_{101}$ and $V_{111}$ are defined as $V_0$, $V_1$, $V_2$, $V_3$, $V_4$, $V_5$, $V_6$ and $V_7$, respectively. By combining Table I and (3)-(5), $\mathrm{d}i_{A,B,C}/\mathrm{d}t$ can be calculated as shown in Table II.

TABLE I
THREE-PHASE VOLTAGES UNDER DIFFERENT BASIC ACTION VECTORS.

| Vector | $u_A$ | $u_B$ | $u_C$ |
|---|---|---|---|
| $V_{000}$ ($V_0$) | 0 | 0 | 0 |
| $V_{100}$ ($V_1$) | $2U_{DC}/3$ | $-U_{DC}/3$ | $-U_{DC}/3$ |
| $V_{110}$ ($V_2$) | $U_{DC}/3$ | $U_{DC}/3$ | $-2U_{DC}/3$ |
| $V_{010}$ ($V_3$) | $-U_{DC}/3$ | $2U_{DC}/3$ | $-U_{DC}/3$ |
| $V_{011}$ ($V_4$) | $-2U_{DC}/3$ | $U_{DC}/3$ | $U_{DC}/3$ |
| $V_{001}$ ($V_5$) | $-U_{DC}/3$ | $-U_{DC}/3$ | $2U_{DC}/3$ |
| $V_{101}$ ($V_6$) | $U_{DC}/3$ | $-2U_{DC}/3$ | $U_{DC}/3$ |
| $V_{111}$ ($V_7$) | 0 | 0 | 0 |

TABLE II
DC-BUS CURRENT AND THREE-PHASE CURRENT DERIVATIVE VALUES UNDER DIFFERENT BASIC ACTION VECTORS.

| Vector | $V_0$ | $V_1$ | $V_2$ | $V_3$ | $V_4$ | $V_5$ | $V_6$ | $V_7$ |
|---|---|---|---|---|---|---|---|---|
| $\mathrm{d}i_A/\mathrm{d}t$ | 0 | $P_1$ | $-P_5$ | $P_4$ | $-P_1$ | $P_5$ | $-P_4$ | 0 |
| $\mathrm{d}i_B/\mathrm{d}t$ | 0 | $P_4$ | $P_6$ | $P_2$ | $-P_4$ | $-P_6$ | $-P_2$ | 0 |
| $\mathrm{d}i_C/\mathrm{d}t$ | 0 | $P_5$ | $-P_3$ | $-P_6$ | $-P_5$ | $P_3$ | $P_6$ | 0 |
| $i_{DC}$ | 0 | $i_A$ | $-i_C$ | $i_B$ | $-i_A$ | $i_C$ | $-i_B$ | 0 |
| $\mathrm{d}i_{DC}/\mathrm{d}t$ | 0 | $P_1$ | $P_3$ | $P_2$ | $P_1$ | $P_3$ | $P_2$ | 0 |
| $P_1$ | $k[L_0-L_2\cos2\theta]$ | | | $P_4$ | $k[-L_0/2-L_2\sin(2\theta-\pi/6)]$ | | | |
| $P_2$ | $k[L_0+L_2\sin(2\theta+\pi/6)]$ | | | $P_5$ | $k[-L_0/2+L_2\sin(2\theta+\pi/6)]$ | | | |
| $P_3$ | $k[L_0-L_2\sin(2\theta-\pi/6)]$ | | | $P_6$ | $k[L_0/2+L_2\cos2\theta]$ | | | |
| $k=2U_{DC}/(3L_dL_q)$ | | | | | | | | |

In Table II, $i_{DC}$ is the DC-bus current, which ~~is equal to different phase current values~~has the same value as that of certain phase current ~~according to~~when applying a specific action vector~~s~~. $P_1$, ..., $P_6$ represent the intermediate variables that indicate current derivative values. From Table II, it can be seen that $i_{DC}$ has two mutually opposite values and the same derivative under opposite basic vectors[NK6], which can be illustrated in Fig.2.

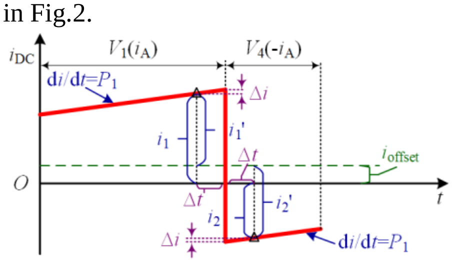


Fig. 2. The DC-bus current under two opposite basic vectors.

In Fig.2, $i_1$ and $i_2$ are the two actual current values ~~two~~ sampled ~~currents~~ under two opposite vectors. ~~If~~ When the offset error, $i_{offset}$, does not exist in the DC-bus current sensor, the two sampled currents are expressed as $i_1'$ and $i_2'$, respectively. Theoretically, $i_2'$ is the ~~negative value~~opposite number of $i_1'$. For t~~T~~he two actual sampled current values $i_1$ and $i_2$~~-~~, the offset error $i_{offset}$ ~~are equal~~is added to the ideal values $i_1'$ and $i_2'$ ~~plus offset error $i_{offset}$~~, respectively. Therefore, $i_{offset}$ can be calculated as the average value of the two actual ~~sampled~~ current values.

By applying the proposed strategy, the DC-bus offset error $i_{offset}$ can be detected and compensated. It can be seen that ~~the proposed method needs~~ only one addition operation and one right shift operation are required in the proposed method (in microprocessors, a one-bit right shift operation is the same as the operation of division by 2), which is very simple. Neither digital filters nor complicated operations are required.

## III. PRINCIPLE OF POSITION SENSOR FAULT DETECTION USING SINGLE DC-BUS CURRENT SENSOR

As displayed in Table II, the DC-bus current derivative ($\mathrm{d}i_{DC}/\mathrm{d}t$) only ~~have~~ has three values ($P_1$, $P_2$ and $P_3$) under different basic vectors. The three derivative values have different relationships with the rotor position. Vectors $V_1$ and $V_4$ are ~~defined as~~classified into "Group-1" because the DC-bus current derivative values are the same ($P_1$) ~~under~~ when applying[NK7] these two vectors. Similarly, vectors $V_3$ and $V_6$ are classified into~~defined as~~ "Group-2", and vectors $V_5$ and $V_2$ are classified into~~defined as~~ "Group-3". Therefore, it is possible to realize position sensor fault detection through DC-bus current slope measurement. By calculation, the rotor position can be obtained by the measured three different DC-bus current derivative values

$$\theta = \left[\arctan 2\left(\sqrt{3}\left(P_2 - P_3\right), \left(-2P_1 + P_2 + P_3\right)\right)\right] / 2 \tag{6}$$

In (6), to obtain the estimated rotor position in a ~~signal~~ single DC-bus current sensor based IPMSM drive system, the three different derivative values of DC-bus current in Table II ($P_1$, $P_2$, and $P_3$) need to be measured within one PWM cycle.

As the offset error of DC-bus current sensor has been calibrated previously, only the effect of scaling error on the position sensor fault detection will be analyzed. The scaling error can be described by the magnification factor $k'$, ~~. Because~~ because the scaling error not only affect the DC-bus current $i_{DC}$, but also affect the reconstructed three-phase currents $i_A$, $i_B$, and $i_C$. [NK8] The magnification factors of all the three-phase currents are the same with that of the DC-bus current factor $k'$. Therefore, coefficients $P_1$, $P_2$, and $P_3$ also share the same magnification factor $k'$. In (6), it can be seen that through arctangent-2 function, the impact of scaling error on position calculation is eliminated.

In Fig.3, the overall scheme of calibration and fault detection for sensors are illustrated. The red dashed line marked with '1' denotes the calibration of the DC-bus current sensor. Whereas the blue dotted line marked with '2' represents the fault detection of the position sensor, where $R$ is the detection result. The calibration of the DC-bus current sensor ~~utilizes~~relies on the sampled current values and the corresponding switching states, which are also utilized to obtain the position/speed estimation results $\theta''/n''$. The speed ~~information~~ $n'$, which is obtained from the position sensor, are also involved in the position sensor fault detection process together with the position signal $\theta'$. The speed ~~information~~ is only utilized as one of the criteria of ~~judgment when~~judging if the sensor fault is ~~recovered or~~ removed. Whereas the position ~~information~~ is applied as the criteria of judgment of both the sensor fault detection and removal.

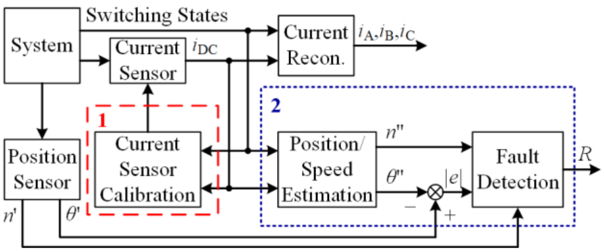


Fig. 3. An overall scheme of calibration and fault detection for sensors.

## IV. Proposed Control Strategies

### A. An Overall Control Scheme

In order to implement the proposed position sensor fault detection scheme using only one DC-bus current sensor with accuracy uncertainty, at least three basic vectors from each of the three defined Groups are required within one PWM cycle. Additionally, an opposite vector of one of the three required basic vectors is also needed for implementing the current sensor accuracy uncertainty calibration strategy. A simple diagram of the proposed control strategy and current sampling method are illustrated in Fig. 4. In the figure, "Vector Group-a/b/c" represents the three defined vector groups in Section III, respectively. It is worth noting that the opposite vector "-$V_a$" in the figure can be either "-$V_b$" or "-$V_c$" according to specific sectors. $T_{min}$ is the minimum period required for precise current measurement after switching the vector. $S_{a1}$, $S_{a2}$, $S_{b1}$, $S_{b2}$, $S_{c1}$, $S_{c2}$ and $i_{a1}$, $i_{a2}$, $i_{b1}$, $i_{b2}$, $i_{c1}$, $i_{c2}$ are the current sampling points and sampled values ~~which~~ that are used for current slope measurement, respectively. In addition, $S_{a2}$, $S_{a2}'$ and $i_{a2}$, $i_{a2}'$ are the two current sampling points and sampled values for DC-bus offset error calibration, respectively. As shown in Fig. 4, the actual DC-bus current during the process of switching cannot follow the ideal one, and the actual current oscillates before it reaches a steady state to track the ideal one. Therefore, a dime[NK9] delay $\Delta t$ ($\Delta t$<$T_{min}$) is required from the switching point to the current sampling point. For accurate measurement of the current slope, the minimum period of 2$T_{min}$ is set for all the three basic vectors. The sum of action time of all the four vectors reaches the switching period $T_s$. The equivalent zero vector is synthesized by the three basic vectors.

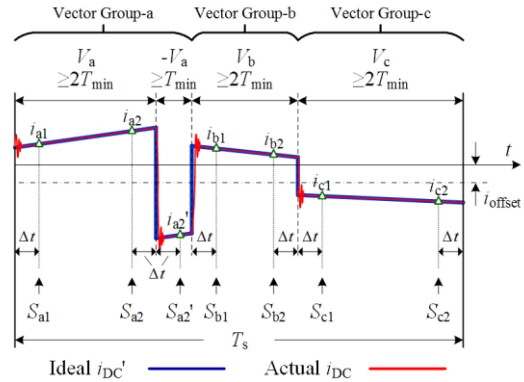

Fig. 4. Simple diagram of the proposed control strategy and current sampling method.

### B. Vector Generation Method and Corresponding Sensor Calibration Strategy

As illustrated in Fig. 4, the action time of the four vectors ~~are no~~is not ~~less~~ shorter than either $T_{min}$ or 2$T_{min}$. ~~And t~~The sum of the four action time is $T_s$. Therefore, the proposed vector generation method and output range is shown in Fig.5.

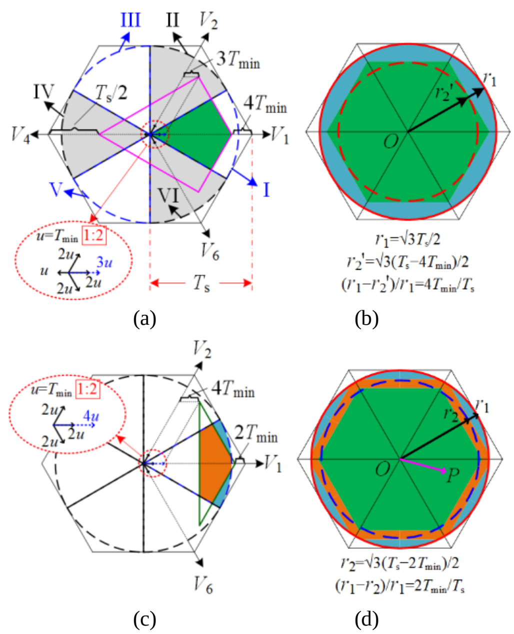

Fig. 5. The proposed vector generation method and output range (with $T_{min}/T_s$=1/20): (a) Vector generation method in defined Sector I, (b) Output voltage range in the six Sectors, (c) Method of expanding the output voltage range in Sector I, (d) Overall output voltage range.

The circular space voltage vector area is divided into six defined sectors in this paper, which are illustrated in Fig.5 (a). The defined six sectors are marked out with roman numerals "I", "II", ..., "VI". The side length of the hexagon is the switching period $T_s$.[NK10] In Sector I, the four vectors $V_1$, $V_2$, $V_4$ and $V_6$ are utilized. The action time of vectors $V_1$, $V_2$ and $V_6$ (defined as $T_{V1}$, $T_{V2}$ and $T_{V6}$, respectively) ~~are~~is not ~~less~~ shorter[NK11] than 2$T_{min}$ and the action time of vector $V_4$ (defined as $T_{V4}$) is less than $T_{min}$. The initial voltage synthesis result is shown in the red dotted circle in the middle, which is magnified by 2 to the red dotted ellipse down to the left-hand side. As shown in the area, ~~a 3$T_{min}$~~ the action time of $V_1$ is 3$T_{min}$~~obtained~~. The remaining action time of the switching period is $T_s$−7$T_{min}$. ~~By applying~~ Distributing the remaining action time to ~~each of~~ the four vectors yields the final voltage output range, which is surrounded by the pink quadrangle. It can be seen that the range of voltage output ~~range~~ covers ~~the~~ most part ~~range~~ of Sector I ~~which~~ that ~~are~~ is indicated by the green shaded part.

By extending the proposed vector synthesis method to the six defined sectors, the whole output voltage range is shown in the greed hexagon in Fig.5 (b). The vector synthesis ~~strategy~~ strategies in the other five sectors are displayed in Table III (Normal Area). As illustrated in Fig.5 (b), the output voltage range (red dashed circle, radius $r_2'$) is minished by 4$T_{min}/T_s$ compared to ~~the output range~~that of the normal voltage synthesis method (red solid circle, radius $r_1$).

TABLE III
VECTOR SYNTHESIS METHOD IN DEFINED SIX SECTORS.

| Sector | | Action time (≥) $T_1$ | $T_2$ | $T_3$ | $T_4$ | $T_5$ | $T_6$ |
|---|---|---|---|---|---|---|---|
| Normal Area | I | 2$T_{min}$ | 2$T_{min}$ | 0 [a] | $T_{min}$ | 0 | 2$T_{min}$ |
| | II | 2$T_{min}$ | 2$T_{min}$ | 2$T_{min}$ | 0 | $T_{min}$ | 0 |
| | III | 0 | 2$T_{min}$ | 2$T_{min}$ | 2$T_{min}$ | 0 | $T_{min}$ |
| | IV | $T_{min}$ | 0 | 2$T_{min}$ | 2$T_{min}$ | 2$T_{min}$ | 0 |
| | V | 0 | $T_{min}$ | 0 | 2$T_{min}$ | 2$T_{min}$ | 2$T_{min}$ |
| | VI | 2$T_{min}$ | 0 | $T_{min}$ | 0 | 2$T_{min}$ | 2$T_{min}$ |
| Extended Area | I | 2$T_{min}$ | 2$T_{min}$ | 0 | 0 | 0 | 2$T_{min}$ |
| | II | 2$T_{min}$ | 2$T_{min}$ | 2$T_{min}$ | 0 | 0 | 0 |
| | III | 0 | 2$T_{min}$ | 2$T_{min}$ | 2$T_{min}$ | 0 | 0 |
| | IV | 0 | 0 | 2$T_{min}$ | 2$T_{min}$ | 2$T_{min}$ | 0 |
| | V | 0 | 0 | 0 | 2$T_{min}$ | 2$T_{min}$ | 2$T_{min}$ |
| | VI | 2$T_{min}$ | 0 | 0 | 0 | 2$T_{min}$ | 2$T_{min}$ |

[a] 0 does not mean that the minimum action time of the corresponding vector is zero but represents that the vector has no action time in such condition.

In order to further extend the output voltage range, in Sector I, the three vectors $V_1$, $V_2$ and $V_6$ are utilized in the area beyond the greed hexagon in Fig.5 (b). $T_{V1}$, $T_{V2}$ and $T_{V6}$ are all set to the values not ~~less~~ smaller than 2$T_{min}$~~.~~, as shown in Fig.5 (c). The initial voltage synthesis result is the part shown in the red dotted circle in the middle, which is magnified by 2 to the red dotted ellipse up to the left-hand side. As shown in the area, ~~a 4$T_{min}$~~ the action time of 4$T_{min}$ is obtained for $V_1$ ~~is obtained~~. Therefore, ~~The~~ the remaining action time of the switching period is $T_s$−6$T_{min}$. The final output voltage range is surrounded by the green triangle. Moreover, ~~The~~ the output voltage range ~~which~~ that is indicated by the orange-colored shaded part covers most ~~range~~ part of Sector I, where the “Normal Area” cannot reach.

By extending the proposed vector synthesis method to the six defined sectors, the whole output voltage range is shown in the orange-colored shaded part in Fig.5 (d). The vector synthesis ~~strategy~~ strategies in the other five sectors are displayed in Table III (Extended Area). As illustrated in Fig.5 (d), the output voltage range (blue dashed circle, radius $r_2$) is minished by 2$T_{min}/T_s$ compared to the output range of the normal voltage synthesis method in Fig.5 (b) (red solid circle, radius $r_1$). Furthermore, ~~The~~ the ~~reduction amount of the~~ output voltage range is reduced by 1-($r_1$-$r_2$)/($r_1$-$r_2'$)=50%.

It is worth noting that the position sensor fault detection strategy can be achieved in both the normal area and the extended ~~area~~one, whereas the DC-bus current sensor calibration strategy can only be realized in the normal area. Although it is a pity to lose the current sensor calibration capability in the extended area, the area is very small, which ~~will~~ hardly ~~have~~ has a great impact on the performance of the system. Besides, as far as the circular output range is considered, the non-extended vector synthesis method will always be used near the center line of each defined sector, making it acceptable for the current sensor calibration strategy ~~which~~ that ~~is~~ does not have extremely high ~~in~~ real-time requirements.

The ~~judging condition~~judgment of whether the output voltage $\boldsymbol{OP}$ ($x_0$, $y_0$) in Fig.5 (d) ~~falling~~ falls in~~to~~ the normal area ($r$=$r_2'$) or the extended area ($r$=$r_2$) is given below

$$\begin{cases} \left|\sqrt{3}x_0 + y_0\right| \le 2r & \sqrt{3}\left|x_0\right| \ge \left|y_0\right| \ \&\ x_0 \cdot y_0 \ge 0 \\ \left|\sqrt{3}x_0 - y_0\right| \le 2r & \sqrt{3}\left|x_0\right| \ge \left|y_0\right| \ \&\ x_0 \cdot y_0 < 0 \\ \left|y_0\right| \le r & \sqrt{3}\left|x_0\right| < \left|y_0\right| \end{cases} \quad (7)$$

## V. EXPERIMENTAL RESULTS

In order to verify the correctness of the proposed DC-bus current sensor offset error calibration strategy and the position fault detection method, an experimental platform is developed as shown in Fig.6. The parameters of the IPMSM used in the experiment are given in Table IV. The drive system is powered by a 380 V three-phase AC voltage source. A rectifier is installed to provide the DC voltage (540 V) for the inverter-an intelligent power module (IPM) (Mitsubishi PM75RLA120), ~~who~~ which served as the PWM voltage source inverter (VSI) with the frequency of 5 kHz ($T_s$ = 200 μs). Also, a ~~multiple~~ multi-level DC output power converter is installed to provide the power for the low voltage devices. An isolated hall-effect current sensor (HS01-100, Max sample rate 100 kHz) is used as the DC-bus current sensor. The offset error value of the DC-bus current sensor is set ~~within~~ in the software of a DSP, TMS320F2812, ~~who~~ which is also utilized to sample the DC-bus current, generate the PWM signals and ~~to~~ implement the proposed sensor calibration strategy, etc. The current clamps are installed for comparison of the currents. A MAGTROL 30 kW dynamometer is utilized for load test. In this paper, $T_{min}$ is set ~~with~~ as 10 μs, and Δ$t$ is set ~~with~~ as 8 μs.

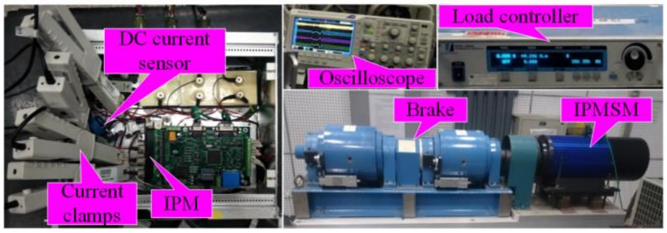


Fig. 6. Experimental setup.

TABLE IV
MAIN PARAMETERS OF IPMSM USED IN EXPERIMENT.

| Parameter | Value | Parameter | Value |
|---|---|---|---|
| Rated power | 5 kW | Pole pairs | 3 |
| Inverter DC voltage | 540 V | *d*-axis Inductance | 4.2 mH |
| Rated voltage | 380 V | *q*-axis Inductance | 10.1 mH |
| Rated current | 8.5 A | Phase resistance | 0.18 Ω |
| Efficiency | 0.9 | Maximum speed | 3000 r/min |
| Rated torque | 15 N·m | | |

In Fig.7, the experimental results of the proposed DC-bus current sensor offset error calibration strategy is illustrated (here, Sector II). In the figure, $i_{DC}$, $i_A$, $i_B$, and $i_C$ are the DC-bus and the actual three-phase currents, $i_A'$, $i_B'$, and $i_C'$ denote the reconstructed three-phase currents, and $i_{offset}$ is artificially added ~~with~~ by -2 A in the controller. The sampled DC-bus current values are displayed in Table V. Therefore, the offset error of the DC-bus current sensor can be calculated as the average of $i_{c2}$ and $i_{c2}'$, which is $i_{offset}'$ = -1.95 A. After ~~the~~ calibration of the DC-bus offset error, the reconstructed three-phase current values can also be obtained as displayed in Table V and illustrated in Fig.7. The reconstructed three-phase currents without calibration of the DC-bus current sensor offset error ($i_A''$, $i_B''$, and $i_C''$) are also given for comparison. It can be seen that the unexpected offset errors in the reconstructed three-phase currents are compensated after calibration of the DC-bus current sensor offset error.

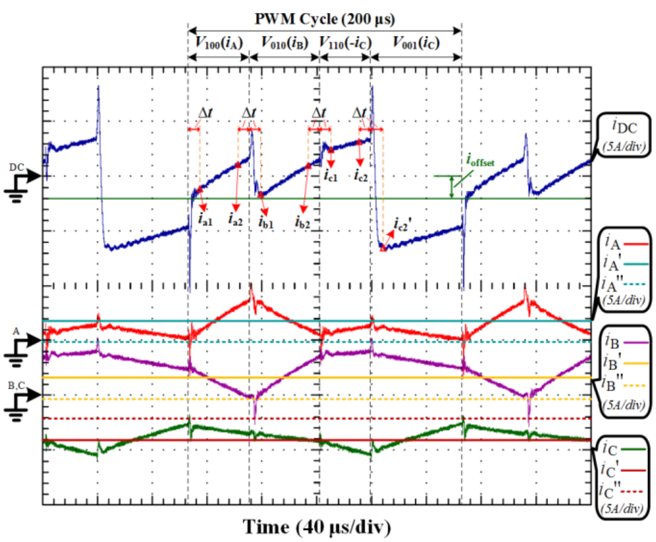


Fig. 7. Experimental results of proposed DC-bus current sensor offset error calibration strategy (here, Sector II).

TABLE V
SAMPLED DC-BUS CURRENT VALUES.

| Current | Value (A) | Current | Value (A) |
|---|---|---|---|
| $i_{a1}$ | -1.35 | $i_{a2}$ | 1.05 |
| $i_{b1}$ | -1.60 | $i_{b2}$ | 0.95 |
| $i_{c1}$ | 2.25 | $i_{c2}$ | 3.00 |
| $i_{c2}'$ | -6.90 | | |
| $i_{offset}'$ | $(i_{c2}+i_{c2}')/2$=-1.95 | $i_A'$ | $(i_{a1}+i_{a2})/2-i_{offset}'$=1.80 |
| $i_B'$ | $(i_{b1}+i_{b2})/2-i_{offset}'$=1.63 | $i_C'$ | $-[(i_{c1}+i_{c2})/2-i_{offset}']$=-4.58 |
| $i_A''$ | $(i_{a1}+i_{a2})/2$ =-0.15 | $i_B''$ | $(i_{b1}+i_{b2})/2$ =-0.33 |
| $i_C''$ | $-(i_{c1}+i_{c2})/2$=-2.63 | | |

Fig.8 illustrates the experimental results of the system performance before and after calibration of the DC-bus current sensor offset error (here, $i_{offset}$=-4 A), which is artificially added to the system by software. In the figure, $T$ and $n$ denote the motor output torque and speed, respectively. $i_d'$ and $i_q'$ are the d- and q-axis motor currents calculated by $i_A'$, $i_B'$, and $i_C'$, respectively. It can be seen that after introduction of the DC-bus current sensor offset error, both the motor output torque and speed fluctuate~~s~~. The error in the reconstructed three-phase current value ~~has more complex kinds of error, which~~ is not only a simple offset error of the current waveform, but also ~~rather the~~contains uncertainty~~ of the error~~. This unexpected error in the reconstructed three-phase currents eventually leads to the fluctuation of the d- and q-axis currents. However, ~~After~~ after ~~the~~ calibration of the DC-bus offset error, all ~~these~~ the unfavorable phenomena ~~have~~ disappear~~ed~~.

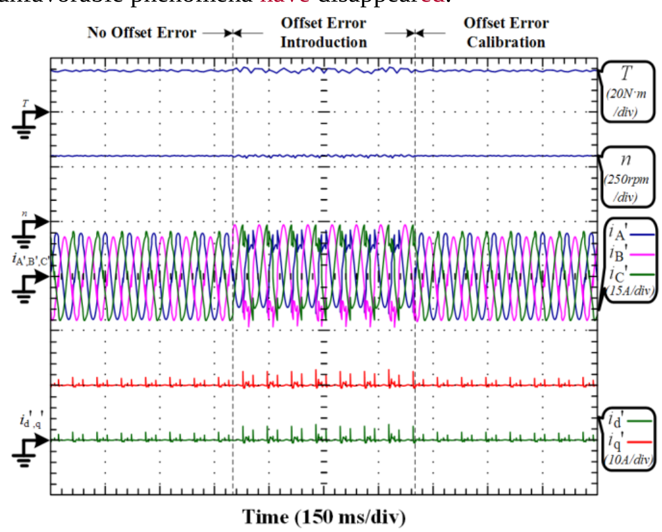


Fig. 8. Experimental results of the system performance before and after calibration of the DC-bus current sensor offset error ($i_{offset}$=-4 A).

The experimental results of the total harmonic distortion (THD) of the actual three-phase currents are displayed in Fig.9. Although the THD level of the proposed method is slightly ~~larger~~ higher than that of the traditional space vector pulse width modulation (SVPWM) method, it is better than or reaches the same level as those of many other PWM synthesis methods [29], [31]. Also, the slightly increased THD does not have a ~~serious~~ significant impact on those large inductive loads [29].

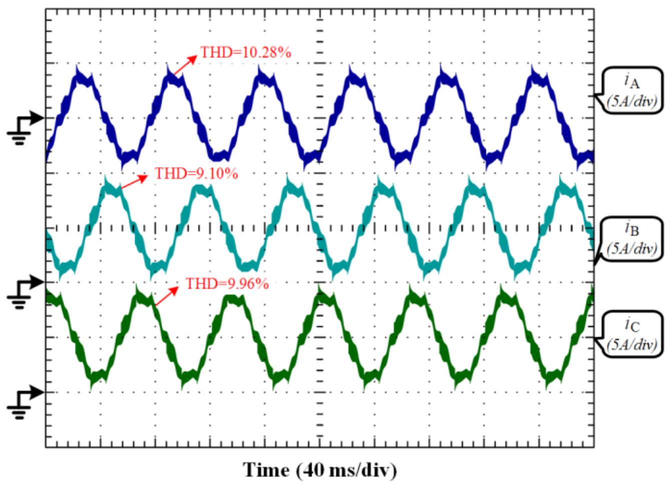


Fig. 9. Experimental results of THD of actual three-phase currents.

Fig.10 shows the experimental results of the system performance at 300rpm and 15 N·m. In Fig.10 (a), the reconstructed three-phase currents track the actual ones accurately. It can be seen that the current fluctuation of both the actual and reconstructed three-phase currents vanished after calibration of the DC-bus current sensor offset error. In Fig.10 (b), $\theta$ and $\theta'_{Re}$ $\Delta\theta'_{Re}$ are the actual and estimated rotor positions, $\Delta\theta'_{Re}$ is the estimation error. The estimation error is controlled within ±0.2 rad in the steady state. Although the error ~~are~~ is not small enough for ~~the~~ sensorless control, it is still sufficient for the purpose of position fault detection ~~purposes~~ for a drive system with position sensor installed.

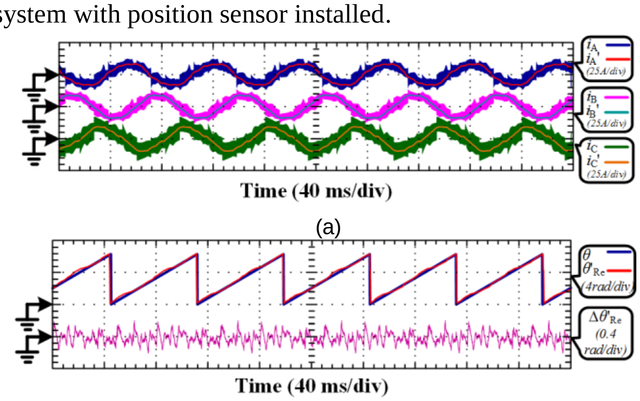


Fig. 10. Experimental results of system performance at 300 rpm and 15 N·m: (a) actual and reconstructed three-phase currents, (b) actual and estimated rotor position.

In Fig.11, the system performance in the starting process ~~are~~ is displayed. It can be seen that during the dynamic process of starting, the reconstructed three-phase currents track the actual ones accurately. Besides, ~~The~~ the position estimation error is controlled within ±0.3 rad in the dynamic process. In Fig.11 (c), the waveforms of the actual and estimated rotor speeds are also given. The estimated rotor speed are calculated ~~using~~ according to the estimated position information. A simple digital low-pass filter is also set as shown in (8) in order to filter out the speed clutters. The estimated rotor speed ~~estimated~~ error ~~are~~ is controlled with ±10 rpm.

$$n[k+1] = Q \cdot n[k] + (1-Q) \cdot \frac{\theta_{Re}'[k+1] - \theta_{Re}'[k]}{T_s} \cdot \frac{30}{\pi p} \quad (8)$$

where $n[k+1]$, $n[k]$, $\theta'_{Re}[k+1]$ and $\theta'_{Re}[k]$, ($k$=1, 2, ...) are the discrete estimated speed and position signals; $Q$ is the filter coefficient; $p$ denotes the rotor pole pairs.

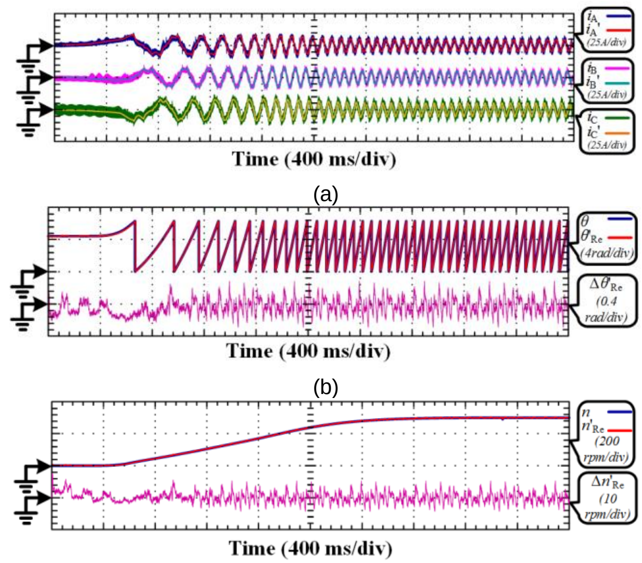


Fig. 11. Experimental results of system performance in the starting process: (a) actual and reconstructed three-phase currents, (b) actual and estimated rotor position, (c) rotor speed.

The system performance in the fast dynamic process (reversing) ~~are~~ is also displayed in Fig.12. The reconstructed three-phase currents track the actual ones accurately. In addition, ~~The~~ the estimated rotor position and speed match the actual ones with an acceptable estimation error.

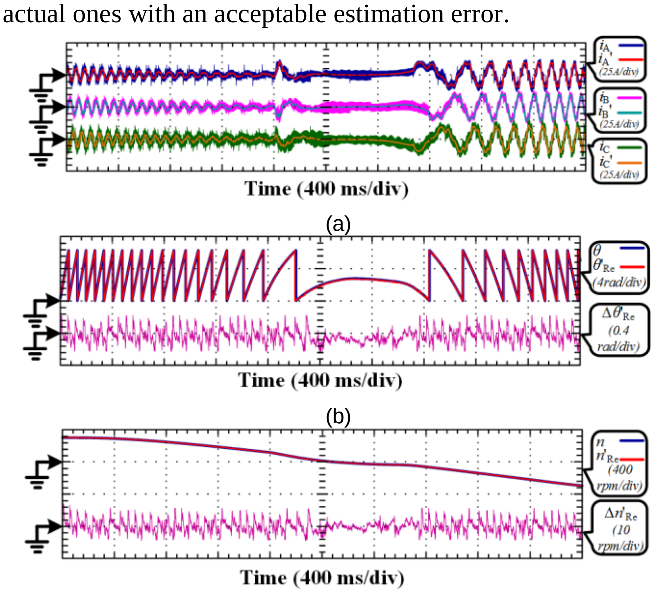


Fig. 12. Experimental results of system performance in the reversing process: (a) actual and reconstructed three-phase currents, (b) actual and estimated rotor position, (c) rotor speed.

The experimental results of the position sensor fault detection are displayed in Fig.13. In the figure, $\theta$ and $\theta'$ are the actual rotor positions before and after introduction of the fault signal, respectively. $\theta''$ is the estimated rotor position obtained from the DC-bus current sensor. $n'$ and $n''$ denote the speed information calculated from $\theta'$ and $\theta''$, respectively. The position sensor fault ~~are~~ is artificially added to the system by software ~~in~~ at point 1 marked with a red arrow. ~~Until point 2, the~~ The fault signal is not detected until reaching point 2, with the value of $|\theta''-\theta'|$ exceeding the preset threshold value (0.4 rad). Upon the detection of the fault signal, depending on the specific requirements of the system, further actions such as fault reporting or sensor isolation and sensorless control switching will be taken. With the ~~rotating~~ rotation of ~~the~~ rotor, the value of $|\theta''-\theta'|$ ~~will be~~becomes smaller than the preset threshold value again (0.4 rad), whilst the sensor fault has not been removed from the system yet. As shown in point 3, the estimated rotor position passed ~~by~~ the actual position with fault signal ($\theta'$). While actually, at point 3 the sensor fault signal still exists.~~,~~ ~~therefore~~Therefore, the speed information calculated ~~from~~ according to $\theta'$ and $\theta''$ ~~are~~ is utilized to dispel the wrong judgment. In this paper, there are two conditions for the judgment of ~~the~~ sensor fault recovery~~ has two conditions~~: (1) The absolute difference between the detected position signal and the estimated value is within the threshold value (0.4 rad) for 10 consecutive cycles, (2) The difference ~~value of~~between the speed values calculated by the detected and the estimated position signals is within ~~another~~ the threshold value ~~(~~of 10 rpm~~)~~. ~~In~~ At point 4, the sensor fault is removed from the system by software, ~~until point 5~~and both the two conditions are satisfied when reaching point 5.~~,~~ At point 5 the sensor isolation is shut off, and the position information is therefore applied in the system again.

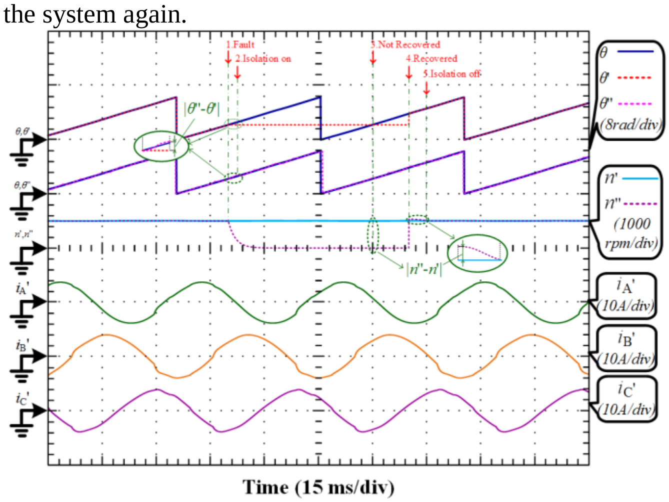


Fig. 13. Experimental results of position sensor fault detection.

## VI. Conclusion

A position sensor fault detection method using a single DC-bus current sensor with accuracy uncertainty in an IPMSM drive system is proposed in this paper. The main contribution of this paper is that the current sensor offset error calibration method and the three-phase current reconstruction process together with the position sensor fault detection strategy are all realized within one single PWM cycle. To accomplish this ~~purpose~~task, the vector generation method is redesigned. The output voltage range is divided into six sectors to ensure the minimum action time of the basic vectors is obtained. Meanwhile, a method of expanding the output voltage range is also developed. Afterwards, two opposite basic vectors are always set together in the non-extended areas to achieve the detection of the DC-bus current sensor offset error. Then the position sensor fault detection strategy is realized by detecting the DC-bus current slopes ~~under~~ when different action vectors are employed. Finally, the effectiveness of the proposed position sensor fault detection method together with the DC-bus current sensor offset error calibration strategy ~~are~~ is verified by the experimental results on a 5-kW IPMSM prototype.

1) The ~~self-calibration~~ detection and self-calibration ~~the detection~~ of the position sensor fault are ~~all~~ both realized by a single DC-bus current sensor.
2) With modulation of the PWM generating method, the DC-bus current sensor offset error calibration strategy, the three-phase current reconstruction process and the position fault detection method can all be achieved by a few current sampling points within one PWM cycle.
3) The DC-bus current sensor offset error calibration method does not need any complicated observers or digital filters, and only the sampled current values are needed.
4) The proposed DC-bus current sensor offset error calibration strategy is applicable but not limited to the IPMSM drive system, and it is widely effective for the motor drive systems ~~which~~ that are driven by PWM based inverters.

## References


[1] Z. Wang, J. Chen, M. Cheng, and Y. Zheng, "Fault-tolerant control of paralleled-voltage-source-inverter-fed PMSM drives," *IEEE Trans. Ind. Electron.*, vol. 62, no. 8, pp. 4749-4760, Aug. 2015.

[2] J. D. Lu, Y. H. Hu, X. K. Zhang, Z. Wang, J. L. Liu, and C. Gan, "High frequency voltage injection sensorless control technique for IPMSMs fed by a three-phase four-switch inverter with a single current sensor," *IEEE/ASME Trans. Mechatronics*, DOI: 10.1109/TMECH.2018.2803772, 2018.

[3] G. L. Wang, D. X. Xiao, N. N. Zhao, X. G. Zhang, W. Wang, and D. G. Xu, "Low-frequency pulse voltage injection scheme-based sensorless control of IPMSM drives for audible noise reduction," *IEEE Trans. Ind. Electron.*, vol. 64, no. 11, pp. 8415-8426, Nov. 2017.

[4] Z. Wang, J. Chen, M. Cheng, and K. T. Chau, "Field-oriented control and direct torque control for paralleled VSIs fed PMSM drives with variable switching frequencies," *IEEE Trans. Power Electron.*, vol. 31, no. 3, pp. 2417-2428, Mar. 2016.

[5] F. R. Salmasi, "A self-healing induction motor drive with model free sensor tampering and sensor fault detection, isolation, and compensation," *IEEE Trans. Ind. Electron.*, vol. 64, no. 8, pp. 6105-6115, Aug. 2017.

[6] M. Kim, S. K. Sul, and J. Lee, "Compensation of current measurement error for current-controlled PMSM drives," *IEEE Trans. Ind. Appl.*, vol. 50, no. 5, pp. 3365-3373, Sep./Oct. 2014.

[7] C. M. Wolf, M. W. Degner, and F. Briz, "Analysis of current sampling errors in PWM VSI drives," *IEEE Trans. Ind. Appl.*, vol. 51, no. 2, pp. 1551-1560, Mar./Apr. 2015.

[8] X. D. Shi and M. Krishnamurthy, "Survivable operation of induction machine drives with smooth transition strategy for EV applications,"

*IEEE J. Emerg. Sel. Topics Power Electron.*, vol. 2, no. 3, pp. 609-617, Sep. 2014.

[9] H. S. Jung, S. H. Hwang, J. M. Kim, C. U. Kim, and C. Choi, "Diminution of current-measurement error for vector-controlled AC motor drives," *IEEE Trans. Ind. Appl.,* vol. 42, no. 5, pp. 1249-1256, Sep./Oct. 2006.

[10] Y. Cho, T. LaBella, and J. S. Lai, "A three-phase current reconstruction strategy with online current offset compensation using a single current sensor," *IEEE Trans. Ind. Electron.,* vol. 59, no. 7, pp. 2924-2933, Jul. 2012.

[11] B. Tabbache, N. Rizzoug, M. E. H. Benbouzid and A. Kheloui, "A control reconfiguration strategy for post-sensor FTC in induction motor-based EVs," *IEEE Trans. Veh. Technol.,* vol. 62, no. 3, pp. 965-971, Mar. 2013.

[12] N. M. A. Freire, J. O. Estima, and A. J. M. Cardoso, "A new approach for current sensor fault diagnosis in PMSG drives for wind energy conversion systems," *IEEE Trans. Ind. Appl.,* vol. 50, no. 2, pp. 1206-1214, Mar./Apr. 2014.

[13] G. Scelba, G. D. Donato, M. Pulvirenti, F. G. Capponi, and G. Scarcella, "Hall-effect sensor fault detection, identification, and compensation in brushless DC drives," *IEEE Trans. Ind. Appl.,* vol. 52, no. 2, pp. 1542-1554, Mar./Apr. 2016.

[14] C. Choi, K. Lee, and W. Lee, "Observer-based phase-shift fault detection using adaptive threshold for rotor position sensor of permanent-magnet synchronous machine drives in electromechanical brake," *IEEE Trans. Ind. Electron.,* vol. 62, no. 3, pp. 1964-1974, Mar. 2015.

[15] A. Raisemche, M. Boukhnifer, C. Larouci and D. Diallo, "Two active fault-tolerant control schemes of induction-motor drive in EV or HEV," *IEEE Trans. Veh. Technol.,* vol. 63, no. 1, pp. 19-29, Jan. 2014.

[16] S. Nalakath, Y. G. Sun, M. Preindl, and A. Emadi, "Optimization-based position sensorless finite control set model predictive control for IPMSMs," *IEEE Trans. Power Electron.,* DOI: 10.1109/TPEL.2017.2784816, 2017.

[17] X. Luo, Q. P. Tang, A. W. Shen, H. L. Shen, and J. B. Xu, "A Combining FPE and Additional Test Vectors Hybrid Strategy for IPMSM Sensorless Control," *IEEE Trans. Power Electron.,* DOI: 10.1109/TPEL.2017.2743106, 2017.

[18] P. L. Xu and Z. Q. Zhu, "Novel square-wave signal injection method using zero-sequence voltage for sensorless control of PMSM drives," *IEEE Trans. Ind. Electron.,* vol. 63, no. 12, pp. 7444-7454, Dec. 2016.

[19] P. L. Xu and Z. Q. Zhu, "Carrier signal injection-based sensorless control for permanent-magnet synchronous machine drives considering machine parameter asymmetry," *IEEE Trans. Ind. Electron.,* vol. 63, no. 5, pp. 2813-2824, May 2016.

[20] M. L. Gu, S. Ogasawara, and M. Takemoto, "Novel PWM schemes with multi SVPWM of Sensorless IPMSM drives for reducing current ripple," *IEEE Trans. Power Electron.,* vol. 31, no. 9, pp. 6461-6475, Sep. 2016.

[21] S. Medjmadj, D. Diallo, M. Mostefai, C. Delpha, and A. Arias, "PMSM drive position estimation: contribution to the high-frequency injection voltage selection issue," *IEEE Trans. Energy Convers.,* vol. 30, no. 1, pp. 349-358, Mar. 2015.

[22] Y. Da, X. D. Shi, and M. Krishnamurthy, "A novel universal sensor concept for survivable PMSM drives," *IEEE Trans. Power Electron.,* vol. 28, no. 12, pp. 5630-5638, Dec. 2013.

[23] C. Chakraborty and V. Verma, "Speed and current sensor fault detection and isolation technique for induction motor drive using axes transformation," *IEEE Trans. Ind. Electron.,* vol. 62, no. 3, pp. 1943-1954, Mar. 2015.

[24] T. A. Najafabadi, F. R. Salmasi and P. J. Maralani, "Detection and isolation of speed-, DC-link voltage-, and current-sensor faults based on an adaptive observer in induction-motor drives," *IEEE Trans. Ind. Electron.,* vol. 58, no. 5, pp. 1662-1672, May 2011.

[25] J. D. Lu, X. K. Zhang, Y. H. Hu, J. L. Liu, C. Gan, and Z. Wang, "Independent phase current reconstruction strategy for IPMSM sensorless control without using null switching states," *IEEE Trans. Ind. Electron.,* vol. 65, no. 6, pp. 4492-4502, June 2018.

[26] Y. X. Xu, H. Yan, J. B. Zou, B. C. Wang, and Y. H. Li, "Zero voltage vector sampling method for PMSM three-phase current reconstruction using single current sensor," *IEEE Trans. Power Electron.,* vol. 32, no. 5, pp. 3797-3807, May, 2017.

[27] X. Li, S. Dusmez, B. Akin, and K. Rajashekara, "A new SVPWM for the phase current reconstruction of three-phase three-level T-type converters," *IEEE Trans. Power Electron.,* vol. 31, no. 3, pp. 2627-2637, Mar. 2016.

[28] Y. S. Lai, Y. K. Lin, and C. W. Chen, "New hybrid pulsewidth modulation technique to reduce current distortion and extend current reconstruction range for a three-phase inverter using only DC-link sensor," *IEEE Trans. Power Electron.,* vol. 28, no. 3, pp. 1331-1337, Mar. 2013.

[29] H. F. Lu, X. M. Cheng, W. L. Qu, S. Sheng, Y. T. Li, and Z. Y. Wang, "A three-phase current reconstruction technique using single DC current sensor based on TSPWM," *IEEE Trans. Power Electron.,* vol. 29, no. 3, pp. 1542-1550, Mar. 2014.

[30] Y. Cho, T. LaBella, and J. S. Lai, "A three-phase current reconstruction strategy with online current offset compensation using a single current sensor," *IEEE Trans. Ind. Electron.,* vol. 59, no. 7, pp. 2924-2933, Jul. 2012.

[31] B. Metidji, N. Taib, L. Baghli, T. Rekioua, and S. Bacha, "Phase current reconstruction using a single current sensor of three-phase AC motors fed by SVM-controlled direct matrix converters," *IEEE Trans. Ind. Electron.,* vol. 60, no. 12, pp. 5497-5505, Dec. 2013.